

# Sensing electric fields through Rydberg atom networks

Philip Kitson,<sup>1,2,3</sup> Wayne J. Chetcuti,<sup>1,4</sup> Gerhard Birkel,<sup>5,6</sup> Luigi Amico,<sup>1,2,3</sup> and Juan Polo<sup>1</sup>

<sup>1</sup>Quantum Research Center, Technology Innovation Institute, P.O. Box 9639 Abu Dhabi, UAE

<sup>2</sup>Dipartimento di Fisica e Astronomia “Ettore Majorana”,

Università di Catania, Via S. Sofia 64, 95123 Catania, Italy

<sup>3</sup>INFN-Sezione di Catania, Via S. Sofia 64, 95123 Catania, Italy

<sup>4</sup>Université Grenoble Alpes, CNRS, LPMMC, 38000 Grenoble, France

<sup>5</sup>Technische Universität Darmstadt, Institut für Angewandte Physik,  
Schlossgartenstraße 7, 64289 Darmstadt, Germany

<sup>6</sup>Helmholtz Forschungsakademie Hessen für FAIR (HFHF),  
GSI Helmholtzzentrum für Schwerionenforschung, 64291 Darmstadt

We present the operating principle of a quantum sensor for electric fields based on networks of Rydberg atoms. The sensing mechanism exploits the dependence of the Rydberg blockade on the electric field, particularly in the vicinity of the Förster resonance - the electric field can be measured through the variation in the size of the blockade radius across the network of Rydberg atoms. Specifically, we track the dynamics of Rydberg excitations in systems of various spatial structures, subjected to different electric field configurations, to monitor the connection between the field and blockade. We also use the density-density correlator to analyse spatially varying (inhomogeneous) electric fields and relate these correlators to the applied fields.

*Introduction* – Rydberg atoms, characterised by electrons occupying states with a high principal quantum number  $n$ , are known to possess unique properties, such as an increased orbital radius (scaling as  $n^2$ ), heightened polarisability ( $n^7$ ), and strong dipole-dipole interactions [1–3]. The dipolar interaction can be effectively scaled as either  $R^{-3}$  or  $R^{-6}$ , depending on the coupled states involved, i.e., states with either opposite or same parity, respectively. These strong interactions can cause shifts in Rydberg energy levels, leading to an excitation blockade effect in nearby atoms when excited with narrow-band radiation [4, 5]. One way to manipulate the atom-atom interactions is by applying an electric field, which results in a differential Stark shift of the levels. Because of the latter, the transitions between *pairs* of Rydberg states, each in different atoms, can become resonant. In this case, an increased strength of resonant dipole-dipole interactions turns out to occur that lead to an enhanced blockade radius. In analogy with the energy transfer originally discussed for organic molecules [6, 7], such a regime is known as a Förster resonance [8–14]. These resonances have been mostly investigated for two atoms (two-body Förster resonances). Efforts have been used to explore three-body Förster resonances [15–19] with applications for three-qubit quantum gates [20] and measurements of the dipole-dipole interaction [21]. Local addressability is also possible using inhomogeneous light fields such as focused laser beams [22].

Clearly, the effect of external fields on atomic systems can provide a physical principle to be exploited in advanced quantum sensing applications [2, 23]. For electric field sensors, Rydberg atoms offer an excellent platform due to their notable polarizability [23–25]. The platform has demonstrated sensitivities of several  $\mu\text{V}/\text{cm}\sqrt{\text{Hz}}$  [26, 27] and can detect fields up to the

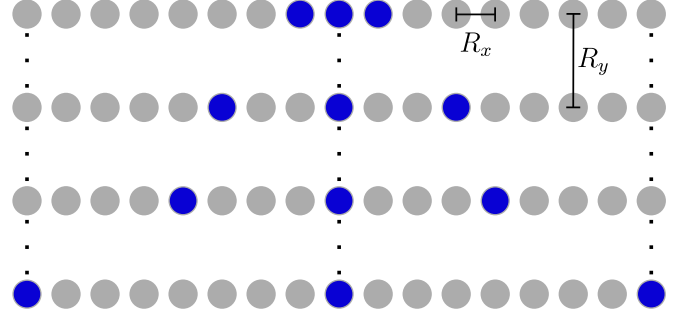


Figure 1. Schematic arrangement of a 2D tweezer array (grey dots) with pitch  $R_x$ . Trapped atoms, which have the possibility to be excited to a Rydberg state, are shown in blue. Each row corresponds to a different atom separation  $R$  in multiples of  $R_x$ . The separation between the rows that are used for measurements fulfils the condition  $R_y \gg R_x$  so that the interaction between atoms in different rows is suppressed. Such a network can be used to sense an electric field  $E$  (constant or spatially dependent) that is applied across the atoms (see the main text for the detailed scheme).

THz range [28, 29]. For scalability and control over interatomic interactions, one can arrange atoms in arrays of optical tweezers generating one-, two-, and three-dimensional (1D, 2D, and 3D) networks [30, 31] of quantum sensors with selectable separations down to the single-micron range (Fig. 1). Recently, a 2D network of individual rubidium atoms has been used as a sensor for a spatially varying magnetic field [32].

In this work, we investigate the working principles for an electric field sensor in a network of Rydberg atoms. We select Rydberg levels for which an external electric field causes the blockade radius to expand when working near Förster resonance. In this scenario, and considering a fixed atom-atom separation, the varying blockade

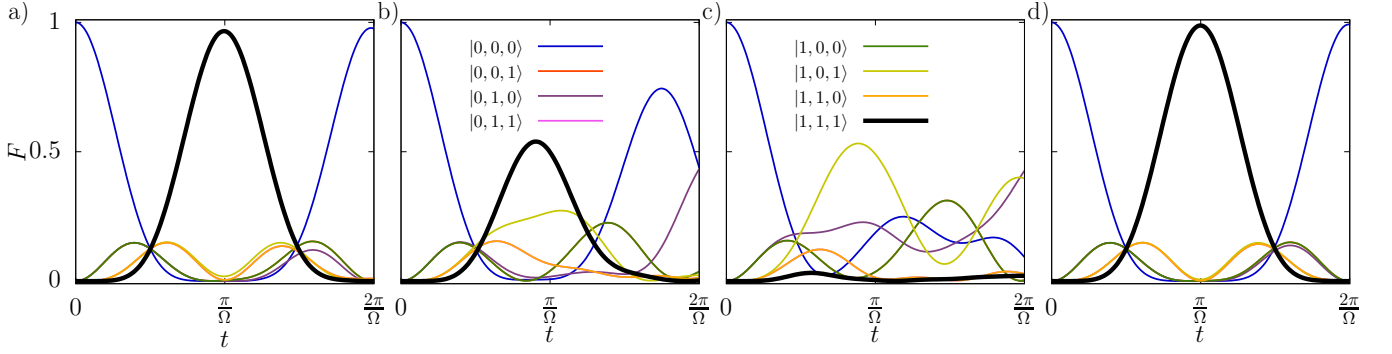


Figure 2. The fidelity  $F$  of the basis states for three interacting atoms having a separation  $R = 15 \mu\text{m}$  over a Rabi period,  $t \in (0, \tau = 2\pi/\Omega)$  for different electric fields  $E$  with  $\Omega$  corresponding to the Rabi frequency. **a)**  $E = 0$  with  $F_{\text{max}} = 0.938$  being the maximum projection over the fully excited state (see Eq. (5)). **b)**  $E = 25 \text{ mV/cm}$  with  $F_{\text{max}} = 0.564$ . **c)**  $E = E_{\text{res}} = 29.787 \text{ mV/cm}$  (corresponding to the resonant electric field) with  $F_{\text{max}} = 0.016$ . **d)**  $E = 50 \text{ mV/cm}$  with  $F_{\text{max}} = 0.978$ .

radius influences the state dynamics. The change in the blockade, in the presence of an electric field, results in a specific state dynamics whose main characteristics can be tracked through the measurement of the population of the fully excited Rydberg state. For spatially varying (inhomogeneous) electric fields, we utilise density-density correlators, which illustrate how the field varies across the atom network.

Based on these concepts, we propose a specific design for an electric field quantum sensor based on a 2D network of Rydberg atoms, as illustrated in Fig. 1. The tweezer array features a horizontal pitch of  $R_x$  and a separation  $R_y$  between the various rows, with  $R_y \gg R_x$  such that interactions between atoms in different rows are suppressed. The number of empty tweezers between adjacent atoms is chosen so that the atoms are regularly spaced with a distance  $R$  between them, which is independently selected for each row in the 2D array. We shall see how this multi-row configuration enables sensing *absolute values* of the electric field, with a sensitivity determined by their pitch separation.

**Models and Methods** – Single atoms with primarily one or two electrons in their outer shell can be driven from the ground  $|g\rangle$  to a Rydberg state  $|\alpha\rangle$  using a resonant field that couples these two states. Assuming a coupling strength characterised by the Rabi frequency  $\Omega$ , the system undergoes Rabi oscillations between the two states [2, 33]. When multiple atoms are driven simultaneously, long-range interactions emerge due to the large dipole moment of Rydberg atoms. For  $N$  atoms, such a system can be modelled via the Hamiltonian [2, 34]

$$H = \frac{\Omega}{2} \sum_i \sigma_i^x - \Delta \sum_i n_i + \sum_{i \neq j}^N V_{i,j} n_i n_j. \quad (1)$$

The Pauli matrices are denoted by  $\sigma_i^u$  (with  $u = x, y, z$ ), and the parameters are  $\Delta$  for the laser detuning and  $V_{i,j}$  for the interaction strength between Rydberg atoms

$i$  and  $j$ . The local number operator defined as  $n_i = \frac{1}{2}(\sigma_i^z + \mathbb{1})$  counts atoms in the Rydberg state. Due to the interaction-induced energy level shift, nearby atoms are prevented from being excited to the Rydberg state – an effect known as the Rydberg blockade [4, 5, 35, 36]. Here we set  $\Delta = 0$  to explore the effects of the blockade.

The Hamiltonian in Eq. (1) describes the physics when an atom is excited to a specific Rydberg state  $|\alpha\rangle$ . We now extend this description to the case where additional nearby Rydberg states are energetically accessible. Consider two identical atoms separated by a distance  $R \equiv R_{1,2}$ , each with available Rydberg states  $|\alpha\rangle$ ,  $|\alpha'\rangle$ , and  $|\alpha''\rangle$ . Whenever the pair state  $|\alpha, \alpha\rangle \equiv |\alpha\rangle_1 \otimes |\alpha\rangle_2$  is nearly degenerate with  $|\alpha', \alpha''\rangle$  and  $|\alpha'', \alpha'\rangle$ , it can couple via the dipole-dipole interaction. In fact, due to the exchange symmetry of the dipole-dipole interaction [14],  $|\alpha, \alpha\rangle$  couples only to the symmetric superposition  $|+\rangle = (|\alpha', \alpha''\rangle + |\alpha'', \alpha'\rangle)/\sqrt{2}$ . Therefore, in the subspace  $\{|\alpha, \alpha\rangle, |+\rangle\}$ , the interaction can be described by an effective two-level Förster Hamiltonian:

$$V^{(\alpha)} = \begin{pmatrix} \delta & C_3/R^3 \\ C_3/R^3 & 0 \end{pmatrix}, \quad (2)$$

where we define the so-called energy defect  $\delta = 2\epsilon_\alpha - \epsilon_{\alpha'} - \epsilon_{\alpha''}$ , with  $\epsilon_\eta$  denoting the single-atom energy of state  $\eta$ . The term  $C_3/R^3$  represents the resonant dipole-dipole matrix element between the pair states, with  $C_3$  being dependent on the dipole matrix elements of the pair states. The effective interaction between two atoms is provided by the lowest energy eigenvalue of Eq. (2):

$$V = \frac{\delta - \sqrt{\delta^2 + 4C_3^2/R^6}}{2}, \quad (3)$$

whereby, the competition between  $\delta$  and  $C_3/R^3$  determines the nature of the interaction term. In the case  $\delta \gg C_3/R^3$ , Eq. (3) can be simplified to  $V \simeq -C_3^2/\delta R^6$ , which

gives rise to Van der Waals-like interactions (VdW). Conversely, if  $\delta \ll C_3/R^3$  then  $V \simeq C_3/R^3$ , resulting in dipole-dipole interactions. When  $\delta \approx C_3/R^3$ , the system undergoes a crossover between the two types of interactions (see Appendix).

In the presence of an electric field  $E$ , the energy levels experience a Stark shift that alters both  $\delta(E)$  and  $C_3(E)$ . Therefore, by gradually increasing the electric field towards the Förster resonance, the nature of interaction changes from VdW to dipole-dipole, *resulting in an enlarged blockade radius* [37]. Here, we consider states that have been previously shown to display a Förster resonance in  $^{87}\text{Rb}$ , e.g.,  $|\alpha\rangle = |59D_{3/2}\rangle$ ,  $|\alpha'\rangle = |61P_{1/2}\rangle$ , and  $|\alpha''\rangle = |57F_{5/2}\rangle$  at the electric field  $E \approx 32$  mV/cm with a magnetic field  $B_z = 3$  G [38]. For these states, we utilise the Alkali Rydberg Calculator (ARC) [39] and obtain  $C_3(E)$  and  $\delta(E)$  at zero magnetic field  $B_z = 0$ . In doing so, we show the relative energies of  $|59D_{3/2}, 59D_{3/2}\rangle$  and  $|57F_{5/2}, 61P_{1/2}\rangle$  in the Appendix.

The time dynamics can be obtained through the Liouville–von Neumann equation:

$$\partial_t \rho(t) = -i [H, \rho(t)], \quad (4)$$

where the density matrix is defined as  $\rho(t) = |\Psi(t)\rangle \langle \Psi(t)|$  with  $|\Psi(t)\rangle$  corresponding to the state of the system. The influence of the electric field is accounted for through the effective interactions Eq. (3) in Eq. (1).

*Dependence of the Rydberg blockade on the electric field* – First, we show how the blockade radius changes under external homogenous electric fields in arrays of Rydberg atoms. We consider an experimentally realistic 2D tweezer network with a fundamental pitch of  $R_x = 5 \mu\text{m}$  (see Fig. 1) in which  $N = 3$  rubidium atoms are placed at a distance  $R = 15 \mu\text{m}$  and subjected to a uniform electric field. The state dynamics in the Fock basis, represented by  $|n_1, \dots, n_N\rangle$  with  $n_i \in 0, 1$ , is shown in Fig. 2 by plotting the fidelity  $F = |\langle n_1, \dots, n_N | \Psi(t) \rangle|^2$  between  $|\Psi(t)\rangle$  and  $|n_1, \dots, n_N\rangle$ . For electric fields far away from the Förster resonance ( $E = 0$  mV/cm (Fig. 2(a)) and  $E = 50$  mV/cm (Fig. 2(d)), the system's population oscillates between the ground and fully excited state  $|1_1, \dots, 1_N\rangle$ , as the resulting blockade radius is smaller than the atom separation. However, for electric fields (e.g.,  $E = 25$  mV/cm (Fig. 2(b))) approaching the Förster resonance, the population of  $|1_1, \dots, 1_N\rangle$  decreases because the energy defect becomes smaller than the coupling strength. Consequently, the blockade radius increases and becomes comparable to the atom separation. At the Förster resonance ( $E = E_{res} = 29.787$  mV/cm with  $B_z = 0$  G (Fig. 2(c))), the blockade radius reaches its maximum value and surpasses the atom separation. As a result, the probability of the system being fully excited drops to nearly zero.

To quantitatively describe the reduction in the probability of the fully excited state around the Förster

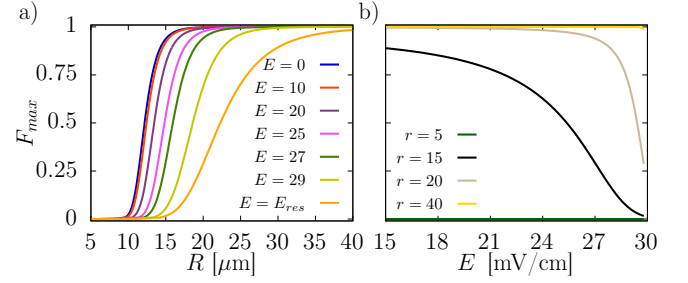


Figure 3. **a)** The maximum fidelity for populating the fully excited state,  $F_{max}$  (Eq. (5)) for  $N = 3$  over the time period  $t \in (0, 2\pi/\Omega)$ . The atoms have a fixed separation which increases from  $R = 5 \mu\text{m}$  to  $R = 40 \mu\text{m}$  for the different electric fields  $E = (0, 10, 20, 25, 27, 29, E_{res})$  mV/cm. **b)**  $F_{max}$  as a function of a uniform electric field across all  $N = 3$  atoms for fixed separations  $R = (5, 15, 20, 40) \mu\text{m}$ .

resonance, we compute the maximum value of the fidelity between  $|\Psi(t)\rangle$  and  $|1_1, \dots, 1_N\rangle$  over a Rabi period  $t \in (0, \tau = 2\pi/\Omega)$  defined as

$$F_{max} = \max_{t \in (0, \tau)} (|\langle 1_1, \dots, 1_N | \Psi(t) \rangle|^2). \quad (5)$$

In Fig. 3(a), we showcase  $F_{max}$  for a uniform electric field across the atoms. At small atom spacings, the value of  $F_{max}$  is small as the blockade radius exceeds the separation. However, as the atom distance increases beyond the blockade radius,  $F_{max}$  also rises. This increase happens at different atom separations as the blockade is larger for electric fields closer to the Förster resonance. Furthermore, the gradient of  $F_{max}$  changes due to the electric field. This is a result of the change in nature of the interactions from  $R^{-3}$  to  $R^{-6}$ , which occurs at short atom-atom separation and more abruptly for  $E = 0$  compared to  $E = E_{res}$  (see more details in the Appendix).

Alternatively, we can look at  $F_{max}$  at fixed atom distances in homogeneous electric fields (Fig. 3(b)). For  $R = 5 \mu\text{m}$ ,  $F_{max}$  remains low for all electric field values as this atom spacing is much smaller than the blockade radius. Conversely, for  $R = 40 \mu\text{m}$ , the separation is much larger than the blockade radius at all electric fields; therefore,  $F_{max}$  remains high. At the intermediate values  $R = 15 \mu\text{m}$  and  $R = 20 \mu\text{m}$   $F_{max}$  decreases as the electric field approaches the Förster resonance, since the blockade exceeds the atom distance. The non-linear behaviour of these curves stems from the way  $F_{max}$  is shifted in Fig. 3(a), which result in a steeper gradient at the larger atom spacings  $R = 20 \mu\text{m}$ .

While  $N = 3$  atoms capture the main features of the Rydberg blockade's dependence on electric field, adding more atoms enhances Rydberg interactions which is reflected in on the blockade radii (see Appendix for other values of  $N$ ).

*Density-Density Correlator* – The main features of the interaction in Rydberg systems are mediated through

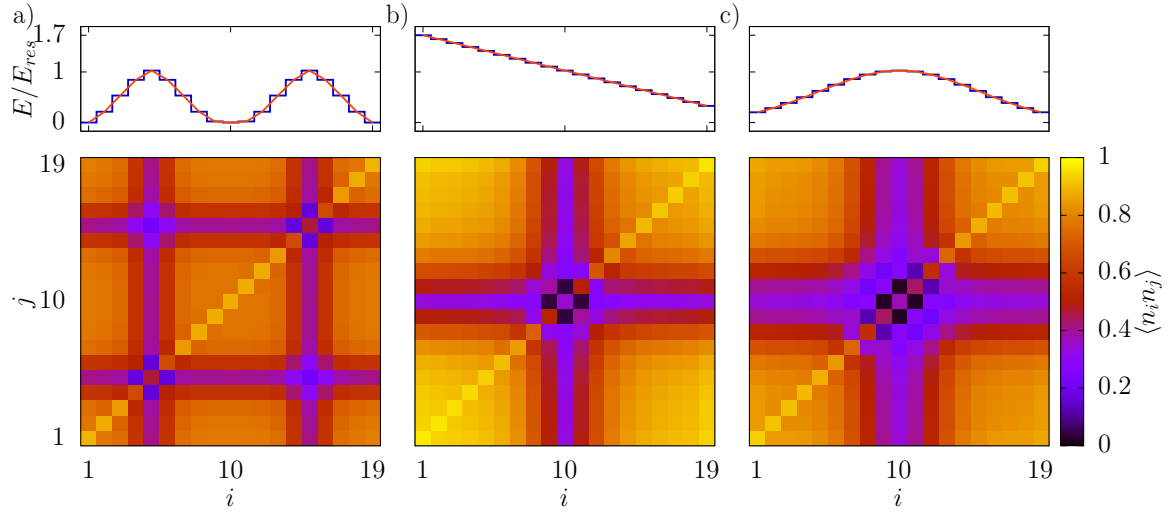


Figure 4. **Top:** The applied electric field configuration  $E/E_{res}$  across  $N = 19$  atoms, which are separated by a distance  $R = 15 \mu\text{m}$ . **Bottom:** The corresponding density-density correlator  $\langle n_i n_j \rangle$  for the above electric field configurations recorded at maximum population of the fully excited state. **a)** Sinusoidal function with two resonant peaks, located at  $i, j = 5$  and  $i, j = 15$ . **b)** Gradient field with  $E = E_{res}$  for atom  $i, j = 10$ . **c)** Gaussian function mimicking the AC Stark shift of a laser beam.

a two-body process; therefore, employing the two-body density-density correlator  $\langle n_i n_j \rangle$  provides deeper insight into the particles' interaction. This quantity serves as a direct and experimentally accessible measure of spatial correlations and offers a clear signature of the Rydberg blockade phenomenon. Our setup relies on the changes of the blockade radius, therefore this measure offers a direct connection to the applied electric fields. To showcase this dependence, we consider a system of  $N = 19$  atoms with an interatomic separation  $R = 15 \mu\text{m}$ , and calculate the correlator for different electric field configurations at the time where the fidelity of the fully excited state ( $|1_1, \dots, 1_{19}\rangle$ ) is maximum, Fig. 4. We note that the diagonal terms represent the expectation value of the density at each site which, for atoms subject to electric fields close to resonance, takes smaller values compared to those with an electric field away from the resonance. Thus, the local density expectation value already provides a signature of the overall shape of the electric field.

The super- and sub-diagonal correlator terms (symmetric under  $i \leftrightarrow j$ ) indicate whether neighbouring atoms can be simultaneously excited. For  $R = 15 \mu\text{m}$ , small  $\langle n_i n_j \rangle$  values signal fields near the Förster resonance, where the blockade radius exceeds the separation and suppresses excitations, while large  $\langle n_i n_j \rangle$  values correspond to fields far from resonance, where multiple excitations are allowed. To illustrate this dependence, in Fig. 4 we consider several electric-field configurations and calculate the resulting correlations. In Fig. 4(a), a spatially sinusoidally varying DC electric field produces correlator minima at resonant positions. A constant negative gradient (Fig. 4(b)) yields nearly equal correlators

about the resonance, though slight differences arise because  $|\delta|$  and  $C_3$  are not fully symmetric with respect to  $\delta = 0$ . Figure 4(c) shows the response to a Gaussian-shaped field, emulating the AC Stark shift from a focused laser beam [22]. All these cases show that  $\langle n_i n_j \rangle$  can capture the overall shape of spatially varying electric fields as this measurement directly reflects interaction-induced spatial correlations.

*Sensing of Electric Fields* – The effects discussed above provide the ingredients for creating a quantum sensor using arrays of Rydberg atoms. Based on the geometry outlined in Fig. 1, we consider a two-dimensional tweezer array with atoms regularly spaced along each row, while the interval between the rows is much larger than the atom-atom separation. Different atom spacings serve as a probe of the distinct blockade radii produced by the specific uniform electric fields. This feature, quantified by the maximum fidelity  $F_{max}$ , can be effectively exploited to get information about the electric field which the atoms experience. We note that, in an experimental setting, the fidelity of state  $|1_1, \dots, 1_N\rangle$  is directly accessible by measuring the Rydberg excitation state of each atom [35, 40]. The flexibility in controlling the geometry can be used to perform multiple measurements in a single shot.

In our scheme, we use different interatomic distances for different rows. While rows with small and large separations ( $R \ll R_b$  and  $R \gg R_b$  at all electric fields such that the dependence is negligible) provide reference baselines for normalisation, intermediate separations—comparable to the number of Rydberg blockade radii over the electric field range—serve as the primary probes for



electric-field sensing. Here, the term baseline refers to reference rows whose response are unaffected by the electric field, thereby providing stable points of comparison when evaluating the sensitivity of the probe rows. This is important for distinguishing genuine field-dependent responses from background fluctuations or systematic offsets produced by spurious external fields such as magnetic gradients. The sensitivity of these sensing channels can range from broad dynamic range to high precision depending on their pitch separation and the applied field as depicted in Fig. 3(b). For example, while  $R = 15 \mu\text{m}$  provides a broad dynamic range for detecting the field  $R = 20 \mu\text{m}$  enables higher sensitivity due to the much larger slope near the Förster resonance  $E \in (27, 30) \mu\text{m}$ . The smallest distance between atoms in our array,  $R = 5 \mu\text{m}$ , and the largest distance, which exceeds the maximum blockade radius obtained at the Förster resonance, e.g.,  $R = 40 \mu\text{m}$ , serve as reference values for normalisation and reduction of the signal-to-noise ratio. Altogether, this configuration enables precise and tunable electric field sensing across a range of field strengths.

For spatially varying electric fields on the micrometre scale, Fig. 4 illustrates how the Rydberg array can reconstruct the overall field profile. In regions where the field is close to the Förster resonance, the correlator  $\langle n_i n_j \rangle$  takes low values, consistent with a blockade radius exceeding the interatomic separation and suppressing simultaneous excitations of neighbouring atoms. In contrast, far from resonance,  $\langle n_i n_j \rangle$  is large, indicating a reduced blockade radius that permits multiple excitations. By mapping these spatial variations in the correlator, the proposed setup can also resolve and characterise local electric-field distributions.

*Conclusion* – In this work, we investigated the Rydberg blockade under both uniform and spatially varying electric fields. The application of an electric field modifies the blockade radius, which reaches its maximum at the Förster resonance owing to the minimisation of an energy defect  $\delta$  between relevant pair states. By employing arrays with tailored interatomic separations, this effect can be exploited to infer the local electric field.

Leveraging this phenomenon, we demonstrate the operating principles of an electric-field sensor based on a two-dimensional Rydberg network, as illustrated in Fig. 1. The sensing mechanism relies on monitoring the maximum fidelity  $F_{\text{max}}$  from Eq. (5), which corresponds to the probability that all atoms in a given row are excited to a Rydberg state - see Ref. [35] for the protocols currently adopted to extract the fidelity in the experiments. For a fixed intra-row distance, the suppression of (or lack of thereof)  $F_{\text{max}}$  provides a direct signature of the local electric field, owing to the strong dependence of the Rydberg blockade radius on the applied field. The network is arranged such that atoms are uniformly spaced within each row, while the inter-row separation is significantly

larger than the intra-row spacing. By engineering distinct intra-row spacings for different rows, the array enables multiple, simultaneous measurements in a single experimental shot: Rows with separations close to the blockade radius exhibit maximal sensitivity to variations in the electric field, whereas rows with large and small separations (much below/above the blockade radius) serve as baseline signals to distinguish the actual signal from fluctuations or systematic offsets.

Complementarily, the density-density correlator  $\langle n_i n_j \rangle$  can provide information about the electric field spatial profile. In particular, low values of  $\langle n_i n_j \rangle$  indicate strong suppression of neighbouring excitations, pointing to an effective interaction enhanced by the presence of a near-resonant electric field.

Together,  $F_{\text{max}}$  and  $\langle n_i n_j \rangle$  serve as indicators of electric fields: the former captures the global suppression patterns indicative of field strength, while the latter reveals local blockade features tied to the spatial profile of the field. While the present implementation is capable of detecting electric fields, its operational range is inherently constrained by the choice of atomic species and the specific Rydberg levels employed. These restrictions arise from the dependence of the blockade radius and level shifts on the principal quantum number and atomic properties. Expanding the dynamic range and enhancing sensitivity could be achieved by incorporating multiple atomic species [41] or by exploiting different Rydberg states within the same array, thereby providing a broader and more tunable response to external electric fields.

Further work could focus on electric fields manipulating Rydberg interactions and the Rydberg blockade. This can be utilised in quantum simulation of models where certain atoms have stronger or weaker interactions, and can be achieved through local addressing of each atom with a designated laser beam.

*Acknowledgements* – We thank Enrico C. Domanti for useful discussions. PK and LA acknowledge the Julian Schwinger Foundation grant JSF-18-12-0011. GB acknowledges financial support by the Federal Ministry of Education and Research (BMBF) [Grants 13N15981 and 13N17366] and by the Deutsche Forschungsgemeinschaft (DFG – German Research Foundation) [Grants BI 647/6-1, BI 647/6-2, and Priority Program SPP 1929 (GiRyd)].

- 
- [1] Wu X, Liang X, Tian Y, Yang F, Chen C, Liu Y C, Tey M K and You L 2021 *Chinese Physics B* **30** 020305 ISSN 1674-1056 URL <http://dx.doi.org/10.1088/1674-1056/abd76f>
  - [2] Adams C S, Pritchard J D and Shaffer J P 2019 *Journal of Physics B: Atomic, Molecular and Optical Physics* **53** 012002 ISSN 1361-6455 URL <http://dx.doi.org/10.1088/1361-6455/ab52ef>

- [3] Gallagher T F 1988 *Reports on Progress in Physics* **51** 143–188 ISSN 1361-6633 URL <http://dx.doi.org/10.1088/0034-4885/51/2/001>
- [4] Jaksch D, Cirac J I, Zoller P, Rolston S L, Côté R and Lukin M D 2000 *Physical Review Letters* **85** 2208–2211 ISSN 1079-7114 URL <http://dx.doi.org/10.1103/PhysRevLett.85.2208>
- [5] Lukin M D, Fleischhauer M, Cote R, Duan L M, Jaksch D, Cirac J I and Zoller P 2001 *Physical Review Letters* **87** ISSN 1079-7114 URL <http://dx.doi.org/10.1103/PhysRevLett.87.037901>
- [6] Förster T 1948 *Annalen der Physik* **437** 55–75 ISSN 1521-3889 URL <http://dx.doi.org/10.1002/andp.19484370105>
- [7] Sahoo H 2011 *Journal of Photochemistry and Photobiology C: Photochemistry Reviews* **12** 20–30
- [8] Anderson W R, Robinson M P, Martin J D D and Gallagher T F 2002 *Physical Review A* **65** ISSN 1094-1622 URL <http://dx.doi.org/10.1103/PhysRevA.65.063404>
- [9] Walker T G and Saffman M 2005 *Journal of Physics B: Atomic, Molecular and Optical Physics* **38** S309–S319 ISSN 1361-6455 URL <http://dx.doi.org/10.1088/0953-4075/38/2/022>
- [10] Vogt T, Viteau M, Chotia A, Zhao J, Comparat D and Pillet P 2007 *Physical Review Letters* **99** ISSN 1079-7114 URL <http://dx.doi.org/10.1103/PhysRevLett.99.073002>
- [11] van Ditzhuijzen C S E, Koenderink A F, Hernández J V, Robicheaux F, Noordam L D and van den Heuvell H B v L 2008 *Physical Review Letters* **100** ISSN 1079-7114 URL <http://dx.doi.org/10.1103/PhysRevLett.100.243201>
- [12] Ryabtsev I I, Tretyakov D B, Beterov I I and Entin V M 2010 *Physical Review Letters* **104** ISSN 1079-7114 URL <http://dx.doi.org/10.1103/PhysRevLett.104.073003>
- [13] Nipper J, Balewski J B, Krupp A T, Butscher B, Löw R and Pfau T 2012 *Physical Review Letters* **108** ISSN 1079-7114 URL <http://dx.doi.org/10.1103/PhysRevLett.108.113001>
- [14] Nipper J, Balewski J B, Krupp A T, Hofferberth S, Löw R and Pfau T 2012 *Phys. Rev. X* **2**(3) 031011 URL <https://link.aps.org/doi/10.1103/PhysRevX.2.031011>
- [15] Faoro R, Pelle B, Zuliani A, Cheinet P, Arimondo E and Pillet P 2015 *Nature Communications* **6** ISSN 2041-1723 URL <http://dx.doi.org/10.1038/ncomms9173>
- [16] Tretyakov D, Beterov I, Yakshina E, Entin V, Ryabtsev I, Cheinet P and Pillet P 2017 *Physical Review Letters* **119** ISSN 1079-7114 URL <http://dx.doi.org/10.1103/PhysRevLett.119.173402>
- [17] Ryabtsev I I, Beterov I I, Tretyakov D B, Yakshina E A, Entin V M, Cheinet P and Pillet P 2018 *Physical Review A* **98** ISSN 2469-9934 URL <http://dx.doi.org/10.1103/PhysRevA.98.052703>
- [18] Cheinet P, Pham K L, Pillet P, Beterov I, Ashkarin I, Tretyakov D, Yakshina E, Entin V and Ryabtsev I 2020 *Quantum Electronics* **50** 213–219 ISSN 1468-4799 URL <http://dx.doi.org/10.1070/QEL17253>
- [19] Ryabtsev I I, Ashkarin I N, Beterov I I, Yakshina E A, Tretyakov D B, Entin V M and Cheinet P 2025 Investigation of three-body förster resonance for various spatial configurations of the three interacting rubidium rydberg atoms URL <https://arxiv.org/abs/2506.22259>
- [20] Beterov I I, Ashkarin I N, Yakshina E A, Tretyakov D B, Entin V M, Ryabtsev I I, Cheinet P, Pillet P and Saffman M 2018 *Physical Review A* **98** ISSN 2469-9934 URL <http://dx.doi.org/10.1103/PhysRevA.98.042704>
- [21] Ryabtsev I I, Ashkarin I N, Beterov I I, Tretyakov D B, Yakshina E A, Entin V M and Cheinet P 2025 Splitting of the three-body förster resonance in rb rydberg atoms as a measure of dipole-dipole interaction strength URL <https://arxiv.org/abs/2507.13658>
- [22] Emperauger G, Qiao M, Bornet G, Chen C, Martin R, Chew Y T, Gély B, Klein L, Barredo D, Browaeys A and Lahaye T 2025 *Physical Review A* **111** ISSN 2469-9934 URL <http://dx.doi.org/10.1103/PhysRevA.111.062806>
- [23] Degen C, Reinhard F and Cappellaro P 2017 *Reviews of Modern Physics* **89** ISSN 1539-0756 URL <http://dx.doi.org/10.1103/RevModPhys.89.035002>
- [24] Zhang H, Ma Y, Liao K, Yang W, Liu Z, Ding D, Yan H, Li W and Zhang L 2024 *Science Bulletin* **69** 1515–1535 ISSN 2095-9273 URL <http://dx.doi.org/10.1016/j.scib.2024.03.032>
- [25] Yuan J, Yang W, Jing M, Zhang H, Jiao Y, Li W, Zhang L, Xiao L and Jia S 2023 *Reports on Progress in Physics* **86** 106001 ISSN 1361-6633 URL <http://dx.doi.org/10.1088/1361-6633/acf22f>
- [26] Facon A, Dietsche E K, Grosso D, Haroche S, Raimond J M, Brune M and Gleyzes S 2016 *Nature* **535** 262–265 ISSN 1476-4687 URL <https://doi.org/10.1038/nature18327>
- [27] Kumar S, Fan H, Kübler H, Jahangiri A J and Shaffer J P 2017 *Optics Express* **25** 8625 ISSN 1094-4087 URL <http://dx.doi.org/10.1364/OE.25.008625>
- [28] Wade C G, Šibalić N, de Melo N R, Kondo J M, Adams C S and Weatherill K J 2016 *Nature Photonics* **11** 40–43 ISSN 1749-4893 URL <http://dx.doi.org/10.1038/nphoton.2016.214>
- [29] Meyer D H, Castillo Z A, Cox K C and Kunz P D 2020 *Journal of Physics B: Atomic, Molecular and Optical Physics* **53** 034001 ISSN 1361-6455 URL <http://dx.doi.org/10.1088/1361-6455/ab6051>
- [30] Pause L, Sturm L, Mittenbühler M, Amann S, Preuschoff T, Schäffner D, Schlosser M and Birkel G 2024 *Optica* **11** 222 ISSN 2334-2536 URL <http://dx.doi.org/10.1364/OPTICA.513551>
- [31] Schlosser M, Tichelmann S, Schäffner D, de Mello D O, Hambach M, Schütz J and Birkel G 2023 *Phys. Rev. Lett.* **130**(18) 180601 URL <https://link.aps.org/doi/10.1103/PhysRevLett.130.180601>
- [32] Schäffner D, Schreiber T, Lenz F, Schlosser M and Birkel G 2024 *PRX Quantum* **5** ISSN 2691-3399 URL <http://dx.doi.org/10.1103/PRXQuantum.5.010311>
- [33] Dunning F B, Killian T C, Yoshida S and Burgdörfer J 2016 *Journal of Physics B: Atomic, Molecular and Optical Physics* **49** 112003 ISSN 1361-6455 URL <http://dx.doi.org/10.1088/0953-4075/49/11/112003>
- [34] Browaeys A and Lahaye T 2020 *Nature Physics* **16** 132–142 ISSN 1745-2481 URL <http://dx.doi.org/10.1038/s41567-019-0733-z>
- [35] Urban E, Johnson T A, Henage T, Isenhower L, Yavuz D D, Walker T G and Saffman M 2009 *Nature Physics* **5** 110–114 ISSN 1745-2481 URL <http://dx.doi.org/10.1038/NPHYS1178>
- [36] Gaëtan A, Miroshnychenko Y, Wilk T, Chotia A, Viteau M, Comparat D, Pillet P, Browaeys A and Grangier P

- 2009 *Nature Physics* **5** 115–118 ISSN 1745-2481 URL <http://dx.doi.org/10.1038/NPHYS1183>
- [37] Reinhard A, Younge K C and Raithel G 2008 *Physical Review A* **78** ISSN 1094-1622 URL <http://dx.doi.org/10.1103/PhysRevA.78.060702>
- [38] Ravets S, Labuhn H, Barredo D, Béguin L, Lahaye T and Browaeys A 2014 *Nature Physics* **10** 914–917 ISSN 1745-2481 URL <http://dx.doi.org/10.1038/nphys3119>
- [39] Šibalić N, Pritchard J, Adams C and Weatherill K 2017 *Computer Physics Communications* **220** 319–331 ISSN 0010-4655 URL <http://dx.doi.org/10.1016/j.cpc.2017.06.015>
- [40] Saffman M, Walker T G and Mølmer K 2010 *Reviews of Modern Physics* **82** 2313–2363 ISSN 1539-0756 URL <http://dx.doi.org/10.1103/RevModPhys.82.2313>
- [41] Otto J S, Kjærgaard N and Deb A B 2020 *Physical review research* **2** 033474
- [42] Wu C E, Kirova T, Auzins M and Chen Y H 2023 *Optics Express* **31** 37094 ISSN 1094-4087 URL <http://dx.doi.org/10.1364/OE.502183>

## APPENDIX: SENSING ELECTRIC FIELDS THROUGH RYDBERG ATOM NETWORKS

### A. Rydberg Interactions, Rydberg Blockade and Förster Resonance

To provide a comprehensive analysis of the Förster resonance, we employ the ARC (Alkali Rydberg Calculator) toolbox to compute relevant data for the Rydberg levels of  $^{87}\text{Rb}$ . Specifically, we consider the pair-states  $|59D_{3/2}, 59D_{3/2}\rangle$  and  $|57F_{5/2}, 61P_{1/2}\rangle$  used in the main text, and evaluate their relative energies  $\epsilon_r$  as a function of an applied electric field in the absence of a magnetic field ( $B_z = 0$  G). The resulting energy difference between the two pair states, referred to as the Förster defect  $\delta(E)$ , varies with the electric field and reaches zero at a particular value, marking the Förster resonance. As shown in Fig. 5, this occurs at an electric field of approximately  $E_{\text{res}} \approx 29.8$  mV/cm. Additionally, the dipole matrix elements  $d_i$  are calculated under each electric field condition, providing the dipole-dipole interaction as

$$C_3(E) = \frac{d_1 d_2}{4\pi\epsilon_0}, \quad (6)$$

where  $\epsilon_0$  is the permittivity of free space. By using both  $C_3(E)$  and  $\delta(E)$  in conjunction with Eq. (3), the energy of the coupled system can be obtained, where an avoided crossing is observed at the Förster resonance.

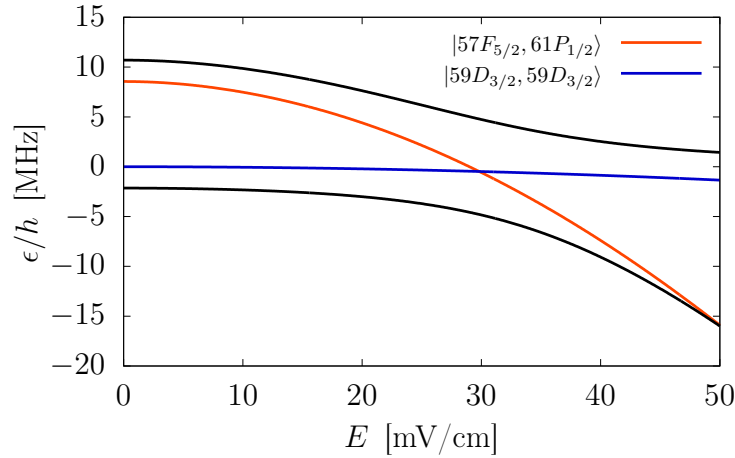


Figure 5. The relative energies  $\epsilon$  in units of the Planck constant  $h$  for the pair states  $|59D_{3/2}, 59D_{3/2}\rangle$  and  $|57F_{5/2}, 61P_{1/2}\rangle$  when coupled (black) and uncoupled (coloured). The two atoms are separated by a distance  $R = 8.1\mu\text{m}$  and magnetic field  $B_z = 0$  G.

Figure 6(a) illustrates how the effective interaction  $V$  varies with the separation between atoms. At short distances, the interaction is strong ( $C_3 > \delta$ ), resulting in a dipole-dipole-like behaviour with  $V \propto R^{-3}$ . As the separation increases and the interaction strength becomes weaker than the energy defect ( $C_3 < \delta$ ), the interaction crosses over to a van der Waals regime, scaling as  $R^{-6}$ . The point at which this transition occurs is identified as the crossover radius,

$$R_c = \left( \frac{C_3}{\hbar|\delta|} \right)^{1/3}, \quad (7)$$

which depends on the applied electric field. The largest value of the crossover radius is observed at the Förster resonance,  $E = E_{\text{res}}$ . This trend is further highlighted in Fig. 6(b), where the crossover radius is plotted as a function of the electric field, showing a pronounced peak at the Förster resonance. For comparison, we also overlay the blockade radius, defined as [42]

$$R_b = \left( \frac{C_6}{\Omega} \right)^{1/6} = \left( \frac{C_3^2}{\hbar|\delta|\Omega} \right)^{1/6}, \quad (8)$$

where the angular component of the interaction is set to 1. Since the blockade radius depends on the energy defect  $\delta$ , it varies with the electric field. As the field approaches the Förster resonance ( $E = E_{\text{res}}$ ),  $\delta \rightarrow 0$  and the blockade radius reaches its maximum value. The nature of the interaction governing the blockade radius can be inferred by comparing it to the crossover radius. When the blockade radius is larger than the crossover radius ( $R_b > R_c$ ), the interaction follows a van der Waals scaling,  $V \propto R^{-6}$ . Conversely, when the blockade radius is smaller than the crossover radius ( $R_b < R_c$ ), the interaction is in the resonant regime and scales as  $V \propto R^{-3}$ —a situation that occurs predominantly near the Förster resonance.

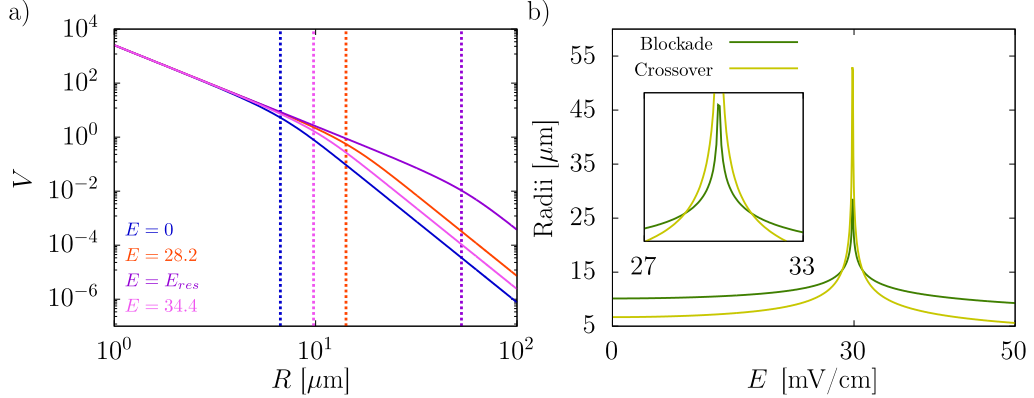


Figure 6. **a)** Effective interaction  $V$  between two Rydberg atoms separated by a distance  $R$  when subjected to electric field  $E = 0$  mV/cm ( $R_c = 6.68 \mu\text{m}$ ),  $E = 28.2$  mV/cm ( $R_c = 14.15 \mu\text{m}$ ),  $E = 29$  mV/cm ( $R_c = 52.95 \mu\text{m}$ ) and  $E = 34.4$  mV/cm ( $R_c = 9.76 \mu\text{m}$ ). The change of behaviour between the dipole-dipole and Van der Waals interaction is recorded as  $R_c$ . **b)** The blockade radius (as defined in Eq. (8)) and the interaction crossover radius,  $R_c$  for different electric fields. The insert zooms into the region between  $E = 27 - 33$  mV/cm.

## B. $F_{\text{max}}$

The collective effect of the Rydberg blockade is examined by computing  $F_{\text{max}}$  for systems with an increasing number of atoms. This serves as an indicator of how the blockade radius evolves with system size. Two electric field values are considered:  $E = 0$  and  $E = E_{\text{res}}$ , with atoms arranged at a fixed separation  $R$ , as illustrated in Fig. 7(a). As more atoms are introduced,  $F_{\text{max}}$  shifts due to the additional interactions in the system. These collective contributions effectively enhance the interaction strength, resulting in an increased blockade radius. The extent of the shift varies with the electric field, as it determines the interaction scaling. At  $E = 0$ , interactions follow a van der Waals scaling ( $V \propto R^{-6}$ ), whereas at the Förster resonance ( $E = E_{\text{res}}$ ), they follow a resonant dipole-dipole scaling ( $V \propto R^{-3}$ ). As a result, the stronger interactions at the resonance lead to a more pronounced shift in  $F_{\text{max}}$  when atoms are added. However, this effect saturates gradually, as atoms farther away contribute less to the total interaction due to the distance dependence.

Furthermore, for fixed atom separations of  $R = 15 \mu\text{m}$  and  $R = 20 \mu\text{m}$ , the increase in blockade radius with the number of contributing atoms is illustrated in Fig. 7(b). At a given electric field,  $F_{\text{max}}$  decreases as the number of



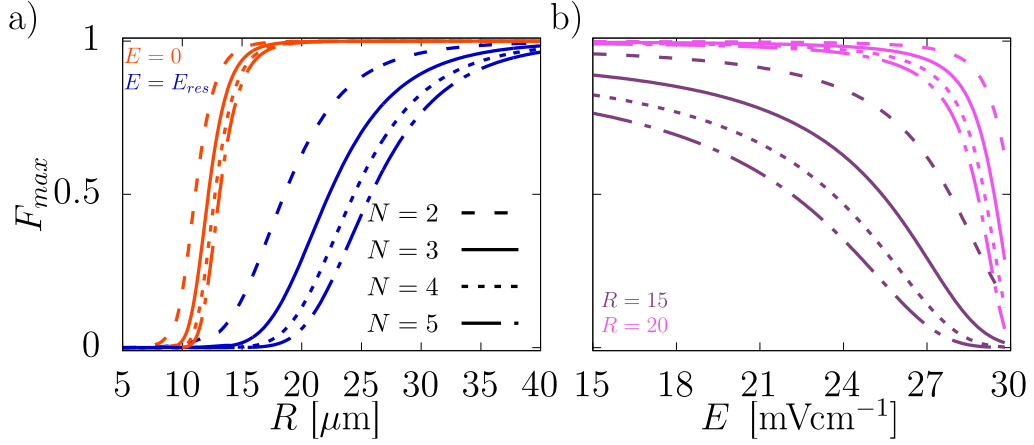


Figure 7. The maximum projection  $F_{max}$  of  $|\Psi\rangle$  to the Fock state  $|1_1, \dots, 1_N\rangle$  over the period  $t \in (0, \tau = 2\pi/\Omega)$  for  $N$  atoms, where  $\Omega$  is the Rabi frequency. **a)** All atoms are subject to the same electric field (either  $E = 0$  or  $E = E_{res}$ ) and have atom separation  $R$ . **b)** All atoms have equal spacing (either  $R = 15 \mu\text{m}$  or  $R = 20 \mu\text{m}$ ) with a uniform applied electric field.

atoms grows. Examining the behaviour of the interaction  $V$  at these separations, we observe that for small electric fields, the interaction scales as  $R^{-6}$ ; however, as the electric field increases, it changes to a  $R^{-3}$  scaling. This crossover occurs at a lower electric field for  $R = 15 \mu\text{m}$  compared to  $R = 20 \mu\text{m}$ , leading to a stronger effect on the blockade radius and thus a more pronounced shift in  $F_{max}$  at the smaller separation.

### C. Density-Density Correlator

The density-density correlator  $\langle n_i n_j \rangle$  is calculated for a system of  $N = 3$  atoms subject to a spatially varying electric field. Results for different electric field configurations are shown in Fig. 8. The diagonal elements represent the excitation probability at each site, while the super- and sub-diagonal elements reflect correlations between nearest neighbours. In configurations where one atom is near the Förster resonance, the correlator with its neighbour is suppressed due to the Rydberg blockade—i.e., the blockade radius exceeds the interatomic separation (as observed in Fig. 8(a,b)). Conversely, when neighbouring atoms are far from resonance, as in Fig. 8(c), the correlators  $\langle n_2 n_3 \rangle$  and  $\langle n_3 n_2 \rangle$  are enhanced, indicating that the blockade is weaker than the separation and simultaneous Rydberg excitation is allowed.

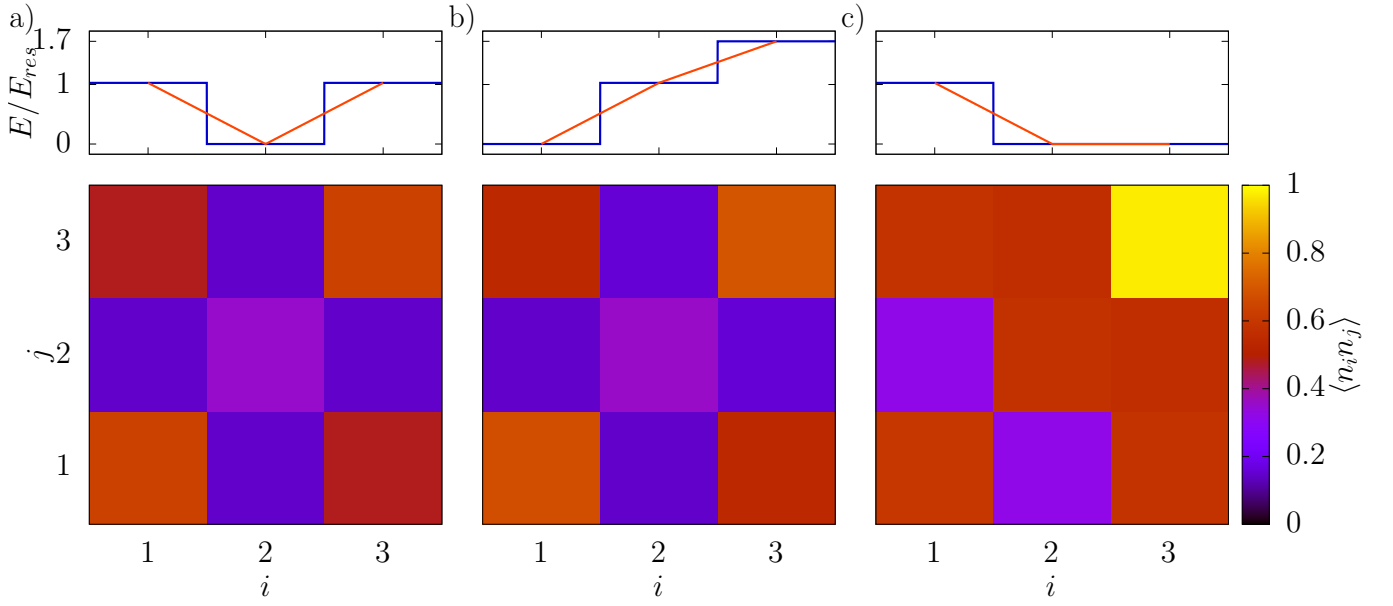


Figure 8. **Top:** The applied electric field configuration  $E/E_{res}$  across  $N = 3$  atoms, which are separated by a distance  $R = 15 \mu\text{m}$ . **Bottom:** The corresponding density-density correlator  $\langle n_i n_j \rangle$  for the above electric field configurations recorded at maximum population of the fully excited state. **a)**  $E/E_{res} = 1, 0, 1$ . **b)**  $E/E_{res} = 0, 1, 1.7$  (where  $E/E_{res} = 1.7$  corresponds to the maximum electric field we consider  $E = 50 \text{ mV/cm}$ ). **c)**  $E/E_{res} = 1, 0, 0$ .